Auranofin induces paraptosis by dual inhibition of thioredoxin reductase and proteasome in breast cancer cells

Min Ji Seo
Ajou University School of Medicine
Dong Min Lee
Ajou University School of Medicine
Hyo Joon Jin
Ajou University School of Medicine
Kyeong Sook Choi (kschoi@ajou.ac.kr)
Ajou University School of Medicine

Article

Keywords: Auranofin, paraptosis, thioredoxin reductase, proteasome, breast cancer

Posted Date: August 25th, 2022

DOI: https://doi.org/10.21203/rs.3.rs-1947663/v1

Version of Record: A version of this preprint was published at Cell Death & Disease on January 19th, 2023. See the published version at https://doi.org/10.1038/s41419-023-05586-6.

Abstract

Auranofin (AF), a gold (I)-containing phosphine compound, is being investigated for oncological application as a repurposed drug. We show here that AF induces paraptosis, a non-apoptotic cell death mode characterized by the dilation of the endoplasmic reticulum (ER) and mitochondria, in breast cancer cells. Although the covalent inhibition of thioredoxin reductase (TrxR), an enzyme that critically controls intracellular redox homeostasis, is considered the primary mechanism of AF's anticancer activity, knockdown of TrxR1 did not induce paraptosis. Instead, TrxR1 knockdown plus the proteasome inhibitor (PI), bortezomib (Bz), or low doses of AF plus Bz induced paraptosis, mimicking the effect of high-dose AF. These results suggest that the paraptosis induced by high-dose AF requires the inhibition of both TrxR1 and proteasome. We found that TrxR1 knockdown/Bz or subtoxic doses of AF and Bz induced paraptosis selectively in breast cancer cells, sparing non-transformed MCF10A cells, whereas high-dose AF killed both cancer and MCF10A cells. GSH depletion was found to be critically involved in the paraptosis induced by dual TrxR1/proteasome inhibition, independent of ROS generation. In this process, the ATF4/CHAC1 (glutathione-specific gamma-glutamylcyclotransferase 1) axis plays a crucial role in GSH degradation, contributing to proteotoxic stress possibly due to accumulation of the misfolded thiol-containing proteins. These results suggest that the paraptosis-inducing strategy of AF plus a PI may provide an effective therapeutic strategy against pro-apoptotic therapy-resistant cancers and reduce the potential side effects by high-dose AF.

Introduction

Auranofin (AF), an FDA-approved antirheumatic drug [1], has been targeted for drug repurposing in anticancer therapy with encouraging results [2]. Reports indicate that thioredoxin reductase (TrxR) is a primary target in the anticancer effect of AF [3, 4, 5]. TrxR (TrxR1 in the cytosol and TrxR2 in mitochondria) is a key member of the thioredoxin (Trx) system, in which TrxR, Trx, and NADPH contribute to redox regulation through forming a reversible disulfide bond [3, 4, 6]. AF may also elicit cytotoxicity in cancer cells by disrupting protein homeostasis (proteostasis) via proteasomal inhibition, in particular, by targeting the 19S proteasome-associated deubiquitinases (DUBs), UCHL5 and USP14 [7, 8, 9]. We show here for the first time that AF induces paraptosis in breast cancer cells by dually targeting TrxR1 and proteasome.

Paraptosis is a non-apoptotic cell death mode accompanied by dilation of the ER and/or mitochondria [10, 11]. Although apoptosis has been considered a major mechanism of chemotherapy-induced cell death, many tumors often develop resistance to most apoptosis-based cancer therapies [12, 13]. Therefore, targeting non-apoptotic forms of cell death, such as paraptosis, may have therapeutic benefits in apoptosis-defective cancer cells. Although the molecular basis of paraptosis remains to be clarified, it has been causatively linked to disruption of proteostasis, such as through inhibition of thiol proteostasis [11, 14, 15, 16, 17] or proteasome [18, 19, 20, 21]. We found that mono-inhibition of TrxR1 or proteasome does not induce anticancer activity; instead, inhibition of both TrxR1 and proteasome is required to induce

paraptosis effectively. These results suggest that high-dose AF-induced paraptosis results from the dual inhibition of TrxR1 and proteasome.

Successful cancer therapy must selectively kill cancer cells while sparing normal cells. High-dose AF was found to kill both breast cancer and non-malignant breast epithelial MCF10A cells, suggesting the potential for side effects in clinical use. In contrast, a combined regimen of low-dose AF plus and the proteasome inhibitor (PI), bortezomib (Bz), or TrxR1 knockdown plus Bz induced paraptosis selectively in breast cancer cells, sparing MCF10A cells. Mechanistically, dual TrxR1/proteasome inhibition upregulates the ATF4/CHAC1 axis to degrade GSH, and thereby contributes to inducing paraptosis by aggravating proteotoxic stress.

Results

Auranofin triggers paraptosis in breast cancer cells

We found that AF treatment dose-dependently induced cell death accompanied by extensive vacuolation in MDA-MB 435S, MDA-MB 231, and BT549 cells, exhibiting IC_{50} values of 4.71 μM, 4.85 μM, and 4.17 μM, respectively (Fig. 1A, B). Unlike TRAIL (an inducer of apoptosis), the application of AF (up to 5 μM) to MDA-MB 435S cells did not induce the cleavage of caspase-3 or its substrate, PARP (Supplementary Fig. 1). Pretreatment with the pan-caspase inhibitor z-VAD-fmk (z-VAD) did not significantly affect AF-induced cell death or vacuolation in all the tested cancer cells (Fig. 1C, D, and Supplementary Fig. 2), suggesting that AF's anticancer effect does not critically depend on apoptosis. Pretreatment with necrostatin-1 (Nec; a necroptosis inhibitor), bafilomycin A1 (Baf; a late-phase autophagy inhibitor), or ferrostatin-1 (Fer; a ferroptosis inhibitor) also did not affect AF-induced cell death and vacuolation in all the tested cancer cells (Fig. 1C, D, and Supplementary Fig. 2). Since paraptotic cell death is accompanied by vacuolation derived from dilation of the ER and/or mitochondria [10, 11], we investigated whether AF induces paraptosis. Observation of the ER and mitochondria employing YFP-ER cells (stably expressing fluorescence in the ER lumen) [18] and MitoTracker-Red (MTR; a fluorescent stain for mitochondria) revealed that untreated cells had the expected reticular-shaped ER and filamentous mitochondria (Fig. 1E), but AF-treated cells exhibited vacuoles derived from dilated ER and mitochondria, a morphological feature of paraptosis. Since paraptosis requires *de novo* protein synthesis [10], we next tested the effect of the protein synthesis blocker, cycloheximide (CHX), on AF-induced cell death. We found that CHX effectively blocked AF-induced cell death and vacuolation in MDA-MB 435S, MDA-MB-231, and BT549 cells (Fig. 1C, E, and Supplementary Fig. 2). CHX also effectively blocked AF-induced vacuolation derived from the ER and mitochondria (Fig. 1E). MAP kinases are associated with paraptosis induced by curcumin [18], celastrol [22], and gambogic acid [15]. We also found that AF activated ERKs, p38, and JNKs in MDA-MB 435S cells (Fig. 1F). These results indicate that AF induces the morphological and biochemical features of paraptosis in these breast cancer cell lines.

AF-induced paraptosis requires inhibition of both TrxR1 and proteasome

Next, we investigated whether AF induces paraptosis via inhibition of TrxR1. TrxR1 knockdown using three independent siRNAs did not alter the viability or morphology of MDA-MB 435S cells (Fig. 2A), suggesting that AF-mediated TrxR1 inhibition would not be enough to trigger paraptosis. Since AF was also shown to inhibit proteasome [7, 8, 9], we examined the involvement of proteasome inhibition in AF-induced paraptosis [7]. An increase in ubiquitylated proteins is a hallmark of proteasome inhibition [23], and 4 ~ 5 μM AF increased the ubiquitylated protein levels, with an effect similar to that of the PI (Bz, 5 nM) (Fig. 2C). We further measured proteasome activity using the Ub^{G76V}-GFP reporter, which contains a single uncleavable N-terminally linked ubiquitin that is attached to GFP and acts as a substrate for polyubiquitination and proteasome-mediated proteolysis [24, 25]. We found that 5 μM AF inhibits proteasome to the same extent as 5 nM Bz (Fig. 2D), whereas TrxR1 knockdown did not affect proteasome activity (Fig. 2C, D). Previously, we reported that proteasome inhibition is necessary but not sufficient to induce paraptosis, suggesting the requirement of other additional signals [19, 20, 26, 27]. Therefore, we examined whether dual TrxR1/proteasome inhibition could mimic AF's paraptosis-inducing activity. We found that while treatment with a PI alone (up to 5 nM Bz or 20 nM carfilzomib (Cfz)) did not notably induce cell death in MDA-MB 435S cells, TrxR1 knockdown plus Bz or Cfz significantly reduced cell viability and induced vacuolation (Fig. 2E, F). CHX, but not inhibitors of the other death modes, effectively inhibited the vacuolation-associated cell death induced by TrxR1 knockdown plus Bz (TrxR1 knockdown/Bz) (Fig. 2G, H). Furthermore, TrxR1 knockdown/Bz, but not either mono-treatment, induced dilation of the ER and mitochondria, and CHX pretreatment effectively inhibited these effects (Fig. 2I). Thus, the co-treatment yielded an effect similar to that obtained with 5 μM AF (Fig. ID, E). These results suggest that AF-induced paraptosis requires inhibition of both TrxR1 and proteasome.

High-dose AF kills breast cancer and non-transformed cells but lower-dose AF/Bz spares normal cells

Next, we tested whether AF preferentially kills cancer cells over normal cells. We found that high-dose (4 ~ 5 μM) AF significantly reduced viability and induced vacuolation also in non-transformed breast epithelial MCF-10A cells (Fig. 3A, B), and thus is not cancer-selective. Treatment of MCF10A cells with 4 μM AF demonstrated cytotoxicity (about 55%) (Fig. 3A) similar to that obtained with 5 μM AF in MDA-MB 435S cells (Fig. 1A). The cell death of MCF10A cells treated with 4 μM AF was significantly inhibited by CHX and weakly, but not significantly, attenuated by z-VAD, Nec, or Fer (Fig. 3C). AF-induced vacuolation was inhibited only by CHX (Fig. 3D). These results suggest that high-dose AF may also induce paraptosis with a possible involvement of a mixed type of cell death in MCF10A cells, whereas it kills MDA-MB 435S cells mainly by inducing paraptosis. Interestingly, the viability and morphology of MCF10A cells were not affected by TrxR1 knockdown or 2 μM AF, in the presence or absence of 5 nM Bz (Fig. 3E-H). These results suggest that combined sub-lethal doses of AF and PI may yield anticancer effects without the cytotoxicity toward normal cells, in contrast to high-dose AF.

Subtoxic doses of AF and PI synergistically induce paraptosis in breast cancer cells

Next, we investigated whether combining low doses of AF and PI induced paraptosis in MDA-MB 435S cells, as seen for TrxR knockdown plus PI. Indeed, sub-lethal doses of AF synergistically reduced cell viability when combined with Bz or Cfz (Fig. 4A). In addition, 2 μM AF dramatically induced vacuolation when combined with 5 nM Bz or 20 nM Cfz (Fig. 4B). Similar results were observed in MDA-MB 231 and BT-549 cells treated with AF plus Bz (Fig. 4A, B), suggesting that the anticancer effect of low-dose AF plus PI may not be restricted to a particular cancer cell line. We also found that 2 μM AF plus 5 nM Bz induced paraptosis in MDA-MB 435S cells, similar to the effect of TrxR1 knockdown plus 5 nM Bz (Fig. 4C-E). In these experiments, 2 μM AF mimicked the paraptosis-sensitizing effect of TrxR1 knockdown in Bz-treated cells (Fig. 2F-I), indicating that 2 μM AF may inhibit TrxR1 as a major target. Collectively, these results suggest that a combination of low-dose AF and PI preferentially kills breast cancer cells by inducing paraptosis, providing a cancer-selective therapeutic strategy that should have fewer side effects than high-dose AF.

GSH depletion is critical for the paraptosis induced by TrxR1/proteasome inhibition

Components of the Trx system, including TrxR1, contribute to rapid proliferation and pro-survival activity in cancer cells, particularly those facing increased oxidative stress [28]. Therefore, we first examined whether ROS generation is critical for the anticancer effect of TrxR1/proteasome inhibition. Staining with CM-H_2DCF-DA to detect ROS generation revealed that H_2O_2 treatment (positive control) increased ROS levels, but no such change was seen for TrxR1 knockdown/Bz or AF/Bz (Fig. 5A). Interestingly, thiol-containing antioxidants, including N-acetylcysteine (NAC) and glutathione reduced ethyl ester (GEE), very effectively blocked the cell death and vacuolation induced by TrxR1 knockdown/Bz, but the non-thiol ROS scavengers, Cu(II)(3,5-diisopropylsalicylate)2 (CuDIPs), and manganese (III) tetrakis (4-benzoic acid) porphyrin chloride (MnTBAP; a superoxide dismutase mimetic), did not (Fig. 5B, C). Since several antioxidants, including ascorbic acid and flavonoids, can directly bind and inactivate Bz [29], we assessed the effects of various antioxidants on the cell death induced by TrxR1/proteasome inhibition employing Cfz instead of Bz. We found that thiol-containing antioxidants, including NAC, GEE, and N-(2-mercapto-propionyl)-glycine (NMPG), but not non-thiol ROS scavengers, such as tiron, ascorbic acid (Vitamin C, AA), CuDIPS, and MnTBAP, markedly inhibited the cell death and vacuolation induced by 2 μM AF plus 20 nM Cfz (Fig. 5D, E). Collectively, these results suggest that ROS generation is not critically involved in this cell death. Since alteration of GSH homeostasis was reportedly correlated with increased AF sensitivity [30], we examined whether inhibition of TrxR1 and/or proteasome altered GSH levels. GSH levels were slightly increased by TrxR1 knockdown or 2 μM AF, slightly decreased by 5 nM Bz alone, and further reduced by TrxR1 knockdown/5 nM Bz or 2 μM AF/5 nM Bz (Fig. 5F). Pretreatment with NAC effectively recovered the GSH levels in cells treated with TrxR1 knockdown/Bz or AF/Bz (Fig. 5G). These results suggest that

the death-blocking effect of thiol antioxidants, including NAC, may reflect the replenishment of intracellular GSH.

ATF4 upregulation critically contributes to the paraptosis induced by TrxR1/proteasome inhibition

The central mechanism of PI-mediated cell death involves the accumulation of toxic poly-ubiquitinated proteins and misfolded protein aggregates (i.e., proteotoxic stress [31, 32]), and PIs activate the integrated stress response (ISR) [33]. Therefore, we examined whether TrxR1 inhibition affects Bz-mediated ISR. We found that treatment with 5 nM Bz slightly increased the expression levels of ISR components, including phosphorylated eIF2α (p-eIF2α), ATF4, and CHOP (Fig. 6A). TrxR1 knockdown or 2 μM AF enhanced the Bz-mediated upregulation of p-eIF2α, ATF4, and CHOP in MDA-MB 435S cells (Fig. 6A), indicating that TrxR1 inhibition enhances Bz-mediated ISR. AF treatment at paraptosis-inducing doses also markedly induced ISR, similar to the effect of TrxR1/proteasome inhibition. ATF4, the core effector of ISR [20, 34], is associated with diverse proteotoxic stress response pathways, including the mitochondrial unfolded protein response (UPR_{mito}) [35, 36] and the ER-unfolded protein response (UPR_{ER}) [37, 38]. CHOP is implicated in the paraptosis induced by dimethoxycurcumin [39] and indirubin-3'-monoxime [40]. When we examined the significance of ATF4 or CHOP, we found that knockdown of ATF4, but not CHOP, remarkably inhibited Bz-induced CHOP upregulation (Fig. 6B) and significantly attenuated the vacuolation-associated cell death induced by TrxR1 knockdown/Bz or AF/Bz (Fig. 6C, D). These results suggest that ATF4 may play a crucial role in the paraptosis induced by TrxR1/proteasome inhibition.

Upregulation of the ATF4/CHAC1 axis is critical for the paraptosis induced by TrxR1/proteasome inhibition through degrading glutathione

Next, we investigated whether ATF4 critically contributes to the paraptosis induced by TrxR1/proteasome inhibition through modulation of its transcriptional target(s). As shown in Fig. 5, down-regulation of GSH was found to be critical for TrxR1/proteasome inhibition-induced paraptosis. Since CHAC1 (glutathione-specific gamma-glutamylcyclotransferase 1), a transcriptional target of ATF4, was shown to degrade GSH by cleaving it to 5-oxo-L-proline and a Cys-Gly dipeptide [41, 42, 43], we investigated the possible involvement of CHAC1 in this cell death. We found that AF dose-dependently increased the protein levels of CHAC1, which paralleled the expression of ATF4 (Fig. 7A). Either TrxR1 knockdown or 2 μM AF further enhanced the Bz-induced upregulation of CHAC1, in parallel with ATF4 upregulation, at the protein and mRNA levels (Fig. 7A, B). ATF4 knockdown effectively inhibited the CHAC1 upregulation induced by TrxR1 knockdown/Bz or AF/Bz at the mRNA and protein levels, whereas CHAC1 knockdown did not affect ATF4 expression (Fig. 7B, C). These results suggest that ATF4 acts upstream of CHAC1. Moreover, CHAC1 knockdown significantly inhibited the cell death and vacuolation caused by TrxR1 knockdown/Bz or AF/Bz (Fig. 7D, E). Knockdown of ATF4 or CHAC1 significantly recovered the GSH levels reduced by TrxR1

knockdown/Bz or AF/Bz (Fig. 7F). These results suggest that the ATF4/CHAC1 axis critically contributes to the paraptosis induced by TrxR1/proteasome inhibition through GSH degradation. We also found that CHX pretreatment effectively restored the GSH levels (Fig. 7G). NAC pretreatment effectively inhibited the upregulation of poly-ubiquitinated proteins, ATF4, and CHAC1 induced by TrxR1 knockdown/Bz or AF/Bz, whereas CHX pretreatment almost completely inhibited these effects (Fig. 7H). Our results suggest that ATF4/CHAC1-mediated GSH degradation may aggravate proteotoxic stress via a vicious cycle. Therefore, dual TrxR1/proteasome inhibition triggers paraptosis by unresolved proteotoxic stress mediated through thiol imbalance. Interestingly, low-dose AF-induced enhancement of Bz-mediated ISR and CHAC1 upregulation observed in MDA-MB 435S cells was not seen in MCF10A cells, suggesting that TrxR1/proteasome inhibition preferentially kills cancer cells via cancer-selective aggravation of proteotoxic stress (Fig. 7I).

In summary, our results reveal that inhibition of both TrxR1 and proteasome is required for AF-induced paraptosis. Compared to high-dose AF, co-treatment with AF and PI at sub-lethal doses may be safer and yield a cancer-selective therapeutic effect. Mechanistically, simultaneous TrxR1/proteasome inhibition triggers ISR via proteotoxic stress that is mediated by ATF4/CHAC1 axis-mediated GSH degradation (Fig. 8).

Discussion

Breast cancer is women's most commonly diagnosed cancer [44]. Although advances in early detection and therapy have significantly improved breast cancer survival rates, most patients develop resistance to the interventions [45]. The major limitations of currently available chemotherapeutics are cancer's drug resistance and toxic side effects [46, 47, 48]. Therefore, there is an unmet clinical need to develop innovative anticancer drugs with improved clinical efficacy and tolerability. In this respect, drug repurposing is a promising and effective strategy [49, 50], and AF, an FDA-approved antirheumatic drug [1], is being investigated for potential therapeutic application in cancer [2]. We show here for the first time that AF induces paraptosis in breast cancer cells via simultaneous inhibition of TrxR1 and proteasome.

TrxRs are selenoproteins with a highly nucleophilic selenocysteine residue at the active site, making them prone to irreversible inhibition by AF even at nanomolar concentrations [3, 4, 5]. In addition to TrxR, proteasome-associated DUBs were implicated in the anticancer effect of AF [7]. Proteasomal inhibition by AF was reported to require 2–3 fold higher doses than that required for TrxR1 inhibition [5]. Here, we show that TrxR1 inhibition by TrxR1 knockdown or 2 μM AF or proteasome inhibition by 5 nM Bz or 20 nM Cfz did not individually kill MDA-MB 435S cells. However, 2 μM AF plus PI or TrxR1 knockdown plus PI effectively induced paraptosis, similar to the effect of 5 μM AF. These results suggest that AF-induced paraptosis requires the dual inhibition of TrxR1 and proteasome.

However, 4 ~ 5 μM AF was cytotoxic to the tested breast cancer and non-malignant MCF10A cells. AF exhibits high reactivity with sulfur- and selenium-ligand proteins having an exposed free cysteine. Therefore, high-dose AF may inhibit multiple targets essential for the survival of normal cells, including

IKK-β [51, 52], STAT3 [53, 54], and protein kinase C iota [55, 56], in addition to TrxR and proteasome. We speculated that a combined regimen could minimize toxicity while optimizing dosing. Indeed, we herein show that, in contrast to high-dose AF, sub-lethal doses of AF and PI were selectively cytotoxic to cancer cells, sparing normal cells.

It is intriguing to speculate on why co-targeting of TrxR1 and proteasome induces cancer-selective paraptosis. Rapidly growing cancer cells exhibit elevated ROS levels and accelerated protein synthesis [57, 58]. TrxR1, a critical modulator of protein redox homeostasis, has emerged as a potential target for cancer therapy, especially in tumor types susceptible to oxidative stress [59]. The proteasome-mediated degradation pathway is an important target for cancer therapy, since proteasome activity is essential for tumor cell proliferation and drug resistance [60, 61]. Therefore, the preferential cytotoxicity of dual TrxR1/proteasome inhibition may reflect the higher dependency of cancer cells on TrxR1 and proteasome to maintain proteostasis. On the other hand, the inability of TrxR1 or proteasome mono-inhibition to kill breast cancer cells may indicate the presence of a cellular backup system and/or resistance mechanisms. In our study, TrxR1 knockdown or 2 μM AF alone slightly increased GSH levels without inducing cell death. A previous study showed that GSH could reduce Trx1 when TrxR1 activity was lost [62], suggesting that GSH may serve as a backup for TrxR1. In addition, tumors lacking TrxR1 were highly susceptible to pharmacological GSH deprivation *in vitro* and *in vivo* [63]. Although PIs are currently used to treat multiple myeloma (MM), most MM patients demonstrate drug-resistant relapse following long-term Bz treatment. Furthermore, the anticancer efficacy of PIs in solid tumors has not been satisfactory [64]. Elevated TrxR1 levels correlate with the acquisition of Bz resistance in MM, and TrxR1 inhibition using AF or TrxR1 silencing reverses Bz resistance [65]. Additionally, increasing GSH levels was shown to abolish Bz-induced cytotoxicity in MM cells [66]. Thus, GSH is causatively linked to the resistance to both TrxR1 and proteasome inhibition. We found that 2 μM AF/Bz or TrxR1 knockdown/Bz induces cell death in breast cancer cells via GSH depletion and upregulation of ISR components. In this process, the ATF4/CHAC1 axis critically contributes to cell-death-related GSH degradation. The NAC-mediated recovery of GSH levels effectively blocked TrxR1/proteasome inhibition-induced ISR and paraptosis. These results suggest that there is a vicious cycle between proteotoxic stress and GSH degradation in the cell death induced by TrxR1/proteasome inhibition. Cytosolic TrxR1 was reported to be critical in reducing non-native disulfides in the ER [67]. Therefore, TrxR1 inhibition could contribute to the misfolding of proteins entering the secretory pathway and the accumulation of misfolded proteins within the ER. GSH also plays a crucial role in native disulfide bond formation within the ER [68], and GSH-dependent proofreading occurs during mitochondrial disulfide-mediated oxidative protein folding [69]. Proteostatic disruption, including impairment of protein thiol homeostasis [11, 14, 15, 16, 17] and proteasomal inhibition [18, 19, 20, 21], has been critically implicated in paraptosis. The vacuolization observed during paraptosis is believed to reflect the influx of water into the ER and mitochondria when osmotic pressure is increased by misfolded proteins accumulated within these organelles [11]. Therefore, TrxR1/proteasome inhibition may trigger proteotoxicity-mediated paraptosis by concomitantly targeting both protein thiol homeostasis and proteasome.

In summary, a combined regimen of reduced doses of AF and Bz may address the potential issues of side effects triggered by high-dose AF and resistance of solid tumors to PI. In addition, the ability of Bz to synergistically enhance the anticancer effects of AF provides a rationale to reposition the latter FDA-approved drug for cancer therapy.

Materials And Methods

Chemicals and antibodies

Chemicals and reagents were obtained as follows: bortezomib (Bz) and carfilzomib (Cfz) from Selleckchem (Houston, TX, USA); Necrostatin-1, bafilomycin A1, N-acetyl-L-cysteine (NAC), and H_2O_2 from Sigma-Aldrich (St Louis, MO, USA); cycloheximide (CHX) and Manganese (III) tetrakis (4-benzoic acid) porphyrin chloride (MnTBAP) from Calbiochem (EDM Millipore Corp., Billerica, MA, USA); Auranofin (AF) from AdipoGen (Liestal, CH, Switzerland); MitoTracker-Red (MTR), propidium iodide (PI), and 5-(and-6)-chloromethyl-2',7'-dichlorofluorescein diacetate (CM-H_2DCF-DA) from Molecular Probes (Eugene, OR, USA); z-VAD-fmk from R&D systems (Minneapolis, MN, USA); Glutathione reduced ethyl ester (GSH-OEt) from Chemodex (Gallen, CH, Switzerland). The following primary antibodies were used: TrxR1 (HPA001395) from Sigma-Aldrich; Ubiquitin (sc-8017) and β-actin (sc-47778) from Santa Cruz Biotechnology (Santa Cruz, CA, USA); ATF4 (#11815), p-eIF2α (#9721), eIF2α (#9722), and CHOP/GADD153 (#2895) from Cell Signaling Technology (Danvers, MA, USA); CHAC1 (15207-1-AP) from Proteintech (Rosemont, IL, USA). The secondary antibodies (rabbit IgG HRP(G-21234) and mouse IgG HRP (G-21040)) were from Molecular Probes.

Cell culture

MDA-MB 435S, MDA-MB 231, BT549, and MCF-10A cells were purchased from American Type Culture Collection (ATCC, Manassas, VA, USA). MDA-MB 435S cells were cultured in DMEM, and MDA-MB 231 and BT549 cells were cultured in RPMI-1640 medium supplemented with 10% fetal bovine serum (FBS) and 1% antibiotics (GIBCO-BRL, Grand Island, NY, USA). MCF-10A cells were maintained in DMEM/F12 supplemented with pituitary extract, insulin, human epidermal growth factor, hydrocortisone, and cholera toxin (Calbiochem). Cells were incubated in 5% CO_2 at 37°C.

Cell viability assay

Cells were cultured in 24-well or 48-well plates and treated as indicated. The cells were then fixed with methanol/acetone (1:1) at − 20°C for 5 min with PBS, and stained with propidium iodide (PI; final concentration, 1 μg/mL) at room temperature for 10 min. The plates were imaged on an IncuCyte device (Essen Bioscience, Ann Arbor, MI, USA) and analyzed using the IncuCyte ZOOM 2016B software. The processing definition of the IncuCyte program was set to recognize attached (live) cells by their red-stained nuclei. The percentage of live cells was normalized to that found in untreated control cultures (100%).

Isobologram analysis

To investigate how the combinations of PIs and AF affected the cancer cell lines, dose-dependent effects were determined for each compound alone and with a fixed concentration of the other co-treated agent. The interactions of the PIs and AF were quantified by determining the combination index (CI), by the following classic isobologram equation: CI = (D)1/(Dx)1 + (D)2/(Dx)2, where (Dx)1 and (Dx)2 indicate the individual doses of PIs and AF, respectively, required to produce an effect, and (D)1 and (D)2 are the doses of PIs and AF, respectively, that produce the same effect when applied in combination. From this analysis, the combined effects of the two drugs can be summarized as follows: CI < 1 indicates synergism; CI = 1 indicates summation (additive and zero interaction); CI > 1 indicates antagonism.

Morphological examination of the ER and mitochondria

The stable cell lines expressing the fluorescence specifically in the ER lumen (YFP-ER cells) were previously described [18]. After treatments, YFP-ER cells were stained with 100 nM MitoTracker-Red (MTR) for 10 min, and morphological changes of the ER and mitochondria were observed under a K1-Fluo confocal laser scanning microscope (Nanoscope Systems, Daejeon, Korea).

Immunoblot analyses

Cells were washed in PBS and lysed in sodium dodecyl sulfate (SDS) sample buffer (125 mM/L Tris [pH6.8], 1% SDS, 20% glycerol, and 2% β-mercaptoethanol). The extracts were boiled for 5 min, separated by SDS-PAGE, and transfected to a Polyvinylidene fluoride membrane (Millipore). After blocking nonspecific binding sites for 30 min with 5% skim milk, membranes were incubated for 1 h with antibodies. Membranes were washed three times with TNET buffer (50 mM Tris-HCl [pH7.4], 150 mM NaCl, 5 mM EDTA, 0.05% Tween20) and incubated further for 1 h with horseradish peroxidase-conjugated anti-rabbit or mouse. Visualization of protein bands was accomplished using ECL (Advansta).

Measurement of proteasome activity employing Ub^{G76V}-GFP

Cells transfected with Ub^{G76V}-GFP were cultured for 48 h in a 24-well plate and treated with the indicated agents for 12 h. The plates were imaged on an IncuCyte device, and the fluorescence intensities were analyzed using the IncuCyte ZOOM 2016B software.

Small interfering RNA-mediated gene silencing

siRNA Negative Control (siNC) (Stealth RNAi™, 12935300) was purchased from Invitrogen (Carsbad, CA, USA). *TrxR1 (TXNRD1)* targeted siRNAs were purchased from Origin (Rockville, MD, USA): siTrxR1 #1 (target sequence GAAUGGACGAUUCCGUCAAGAGAUA); siTrxR1 #2 (target sequence CAGCAGUGAUGAUCUUUUCUCCUUG); siTrxR1 #3 (target sequence ACAAGUACAUCUGCGAUCAACUCTA) (SR304982). *ATF4 (CREB-2)* targeted siRNA was from Santa Cruz: siATF4 (target sequence CCACUCCAGAUCAUUCCUU, GGAUAUCACUGAAGGAGAU, and GUGAGAAACUGGAUAAGAA, sc-35112). *CHOP (DDIT3)* targeted siRNA was synthesized from Invitrogen: siCHOP (target sequence GAGCUCUGAUUGACCGAAUGGUGAA). *CHAC1* targeted siRNA was synthesized from Genolution (Seoul,

Korea): siCHAC1 (target sequence GAUCAUGAGGGCUGCACUU). The pairs of siRNA oligonucleotides were annealed and transfected to cells using the RNAiMAX reagent (Invitrogen), according to the manufacturer's instructions. To confirm successful siRNA-mediated knockdown, Western blotting of the proteins of interest was performed.

Measurement of reactive oxygen species (ROS) generation

Treated cells were incubated with 10 μM of CM-H_2DCF-DA for 30 min at 37°C, and subjected to fluorescence microscopy. Images were acquired from Axiovert 200M fluorescence microscope using Zeiss filter sets #46 (excitation band pass, 500/20 nm; emission band pass, 535/30 nm).

Measurement of intracellular GSH levels

Intracellular GSH levels were analyzed using a Glutathione Assay kit (Cayman, Michigan, USA). MDA-MB 435S cells plated to 6-well plates (20 x 10^4 cells/well) were treated with AF and/or Bz for 12 h, washed with PBS, trypsinized, and centrifuged at 2,000 x g for 10 min at 4°C. Cells were lysed by sonication in 1X MES buffer (0.2 M 2-(N-morpholino)methanesulfonic acid, 0.5 mM K_2HPO_4, 1 mM EDTA (pH 6.0)) and centrifuged. Samples were then mixed with an equal volume of 0.1 μg/ml metaphosphoric acid and centrifuged to precipitate protein; and 200 mM triethanolamine was added to supernatants. Samples were then transferred to a 96-well plate (50 μL/well) and the reaction was started by adding assay buffer with GSH reaction mixture (containing NADP+, glucose-6-phosphate, glucose-6-phosphate reductase, glutathione reductase, and 5,5'-dithiol-bis-2-nitrobenzoic acid). Production of 5-thio-2- nitrobenzoic acid was measured for 25 min using a microplate reader (Synergy2, BioTek, Winooski, VT, USA). A portion of lysate, taken from before protein precipitation, was set to determine protein concentration.

RNA isolation and quantitative real-time RT-PCR (qRT-PCR)

Total RNA was isolated from MDA-MB 435S cells transfected with siNC, siTrxR1, siATF4, or siCHAC1 by using TRIzol® reagent (10296010, Thermo Scientific (Waltham, MA, USA)), according to the manufacturer's instructions. To perform quantitative real-time RT-PCR (qRT-PCR), cDNA was synthesized from 1 μg of total RNA of each sample using an M-MLV cDNA Synthesis kit (EZ006S, Enzynomics (Daejeon, Korea)). qRT-PCR was performed using a Bio-Rad Real-Time PCR System (Bio-Rad, Richmond, CA, USA). Relative expression levels were determined with the ΔΔCt method [70] and normalized to the mean of the housekeeping gene GAPDH. All primer sequences of qRT-PCR were listed in Supplementary Table 1.

Statistical analysis

All data are presented as mean ± SD (standard deviation) from at least three separate experiments. To perform statistical analysis, GraphPad Prism (GraphPad Software Inc, Sandiego, CA) was used. Normality of data was assessed by Kolmogorov–Smirnov testes and equal variance using Bartlett's test. For a normal distribution, statistical differences were determined using an analysis of variance (ANOVA) followed by Bonferroni multiple comparison test. If the data were not normally distributed, Kruskal–Wallis test was performed followed by Dunn's test. * $p < 0.05$ was considered statistically significant.

Declarations

Funding

This work was supported by the National Research Foundation of Korea (NRF) grants funded by the Korean government, Mid-career Research Program (NRF-2020R1A2C1013562).

Author contribution

M.J.S and H.J.J performed experiments; D.M.L provided technical and material support; M.J.S and K.S.C performed study design and writing.

Ethics declarations

Conflict of interests

The authors declare no conflict of interest.

Data availability

All data and information concerning this study will be made available upon request.

References

1. Finkelstein AE, Walz DT, Batista V, Mizraji M, Roisman F, Misher A. Auranofin. New oral gold compound for treatment of rheumatoid arthritis. Ann Rheum Dis 1976, **35**(3): 251–257.
2. Gamberi T, Chiappetta G, Fiaschi T, Modesti A, Sorbi F, Magherini F. Upgrade of an old drug: Auranofin in innovative cancer therapies to overcome drug resistance and to increase drug effectiveness. Med Res Rev 2022, **42**(3): 1111–1146.
3. Rackham O, Shearwood AM, Thyer R, McNamara E, Davies SM, Callus BA, *et al.* Substrate and inhibitor specificities differ between human cytosolic and mitochondrial thioredoxin reductases: Implications for development of specific inhibitors. Free Radic Biol Med 2011, **50**(6): 689–699.
4. Gandin V, Fernandes AP, Rigobello MP, Dani B, Sorrentino F, Tisato F, *et al.* Cancer cell death induced by phosphine gold(I) compounds targeting thioredoxin reductase. Biochem Pharmacol 2010, **79**(2): 90–101.
5. Zhang X, Selvaraju K, Saei AA, D'Arcy P, Zubarev RA, Arnér ES, *et al.* Repurposing of auranofin: Thioredoxin reductase remains a primary target of the drug. Biochimie 2019, **162**: 46–54.
6. Zhang J, Li X, Han X, Liu R, Fang J. Targeting the Thioredoxin System for Cancer Therapy. Trends Pharmacol Sci 2017, **38**(9): 794–808.
7. Liu N, Li X, Huang H, Zhao C, Liao S, Yang C, *et al.* Clinically used antirheumatic agent auranofin is a proteasomal deubiquitinase inhibitor and inhibits tumor growth. Oncotarget 2014, **5**(14): 5453–5471.

8. Lee S, Kim SM, Lee RT. Thioredoxin and thioredoxin target proteins: from molecular mechanisms to functional significance. Antioxid Redox Signal 2013, **18**(10): 1165–1207.
9. Chiappetta G, Gamberi T, Faienza F, Limaj X, Rizza S, Messori L, *et al.* Redox proteome analysis of auranofin exposed ovarian cancer cells (A2780). Redox Biol 2022, **52**: 102294.
10. Sperandio S, de Belle I, Bredesen DE. An alternative, nonapoptotic form of programmed cell death. Proc Natl Acad Sci U S A 2000, **97**(26): 14376–14381.
11. Lee D, Kim IY, Saha S, Choi KS. Paraptosis in the anti-cancer arsenal of natural products. Pharmacol Ther 2016, **162**: 120–133.
12. Constantinou C, Papas KA, Constantinou AI. Caspase-independent pathways of programmed cell death: the unraveling of new targets of cancer therapy? Curr Cancer Drug Targets 2009, **9**(6): 717–728.
13. Kolenko VM, Uzzo RG, Bukowski R, Finke JH. Caspase-dependent and -independent death pathways in cancer therapy. Apoptosis 2000, **5**(1): 17–20.
14. Kim IY, Kwon M, Choi MK, Lee D, Lee DM, Seo MJ, *et al.* Ophiobolin A kills human glioblastoma cells by inducing endoplasmic reticulum stress via disruption of thiol proteostasis. Oncotarget 2017, **8**(63): 106740–106752.
15. Seo MJ, Lee DM, Kim IY, Lee D, Choi MK, Lee JY, *et al.* Gambogic acid triggers vacuolization-associated cell death in cancer cells via disruption of thiol proteostasis. Cell Death Dis 2019, **10**(3): 187.
16. Binoy A, Nedungadi D, Katiyar N, Bose C, Shankarappa SA, Nair BG, *et al.* Plumbagin induces paraptosis in cancer cells by disrupting the sulfhydryl homeostasis and proteasomal function. Chem Biol Interact 2019, **310**: 108733.
17. Hager S, Korbula K, Bielec B, Grusch M, Pirker C, Schosserer M, *et al.* The thiosemicarbazone Me(2)NNMe(2) induces paraptosis by disrupting the ER thiol redox homeostasis based on protein disulfide isomerase inhibition. Cell Death Dis 2018, **9**(11): 1052.
18. Yoon MJ, Kim EH, Lim JH, Kwon TK, Choi KS. Superoxide anion and proteasomal dysfunction contribute to curcumin-induced paraptosis of malignant breast cancer cells. Free Radic Biol Med 2010, **48**(5): 713–726.
19. Lee DM, Kim IY, Seo MJ, Kwon MR, Choi KS. Nutlin-3 enhances the bortezomib sensitivity of p53-defective cancer cells by inducing paraptosis. Exp Mol Med 2017, **49**(8): e365.
20. Lee DM, Seo MJ, Lee HJ, Jin HJ, Choi KS. ISRIB plus bortezomib triggers paraptosis in breast cancer cells via enhanced translation and subsequent proteotoxic stress. Biochem Biophys Res Commun 2022, **596**: 56–62.
21. Lee HJ, Lee DM, Seo MJ, Kang HC, Kwon SK, Choi KS. PSMD14 Targeting Triggers Paraptosis in Breast Cancer Cells by Inducing Proteasome Inhibition and Ca(2+) Imbalance. Int J Mol Sci 2022, **23**(5).
22. Yoon MJ, Lee AR, Jeong SA, Kim YS, Kim JY, Kwon YJ, *et al.* Release of Ca2 + from the endoplasmic reticulum and its subsequent influx into mitochondria trigger celastrol-induced paraptosis in cancer

cells. Oncotarget 2014, **5**(16): 6816–6831.

23. Menéndez-Benito V, Verhoef LG, Masucci MG, Dantuma NP. Endoplasmic reticulum stress compromises the ubiquitin-proteasome system. Hum Mol Genet 2005, **14**(19): 2787–2799.
24. Johnson ES, Ma PC, Ota IM, Varshavsky A. A proteolytic pathway that recognizes ubiquitin as a degradation signal. J Biol Chem 1995, **270**(29): 17442–17456.
25. Dantuma NP, Lindsten K, Glas R, Jellne M, Masucci MG. Short-lived green fluorescent proteins for quantifying ubiquitin/proteasome-dependent proteolysis in living cells. Nat Biotechnol 2000, **18**(5): 538–543.
26. Yoon MJ, Kim EH, Kwon TK, Park SA, Choi KS. Simultaneous mitochondrial Ca(2+) overload and proteasomal inhibition are responsible for the induction of paraptosis in malignant breast cancer cells. Cancer Lett 2012, **324**(2): 197–209.
27. Lee AR, Seo MJ, Kim J, Lee DM, Kim IY, Yoon MJ, *et al.* Lercanidipine Synergistically Enhances Bortezomib Cytotoxicity in Cancer Cells via Enhanced Endoplasmic Reticulum Stress and Mitochondrial Ca(2+) Overload. Int J Mol Sci 2019, **20**(24).
28. Jovanović M, Podolski-Renić A, Krasavin M, Pešić M. The Role of the Thioredoxin Detoxification System in Cancer Progression and Resistance. Front Mol Biosci 2022, **9**: 883297.
29. Zou W, Yue P, Lin N, He M, Zhou Z, Lonial S, *et al.* Vitamin C inactivates the proteasome inhibitor PS-341 in human cancer cells. Clin Cancer Res 2006, **12**(1): 273–280.
30. Yan X, Zhang X, Wang L, Zhang R, Pu X, Wu S, *et al.* Inhibition of Thioredoxin/Thioredoxin Reductase Induces Synthetic Lethality in Lung Cancers with Compromised Glutathione Homeostasis. Cancer Res 2019, **79**(1): 125–132.
31. Peters JM. Proteasomes: protein degradation machines of the cell. Trends Biochem Sci 1994, **19**(9): 377–382.
32. Dantuma NP, Lindsten K. Stressing the ubiquitin-proteasome system. Cardiovasc Res 2010, **85**(2): 263–271.
33. Obeng EA, Carlson LM, Gutman DM, Harrington WJ, Jr., Lee KP, Boise LH. Proteasome inhibitors induce a terminal unfolded protein response in multiple myeloma cells. Blood 2006, **107**(12): 4907–4916.
34. Pakos-Zebrucka K, Koryga I, Mnich K, Ljujic M, Samali A, Gorman AM. The integrated stress response. EMBO Rep 2016, **17**(10): 1374–1395.
35. Melber A, Haynes CM. UPR(mt) regulation and output: a stress response mediated by mitochondrial-nuclear communication. Cell Res 2018, **28**(3): 281–295.
36. Sasaki K, Uchiumi T, Toshima T, Yagi M, Do Y, Hirai H, *et al.* Mitochondrial translation inhibition triggers ATF4 activation, leading to integrated stress response but not to mitochondrial unfolded protein response. Biosci Rep 2020, **40**(11).
37. Rozpedek W, Pytel D, Mucha B, Leszczynska H, Diehl JA, Majsterek I. The Role of the PERK/eIF2α/ATF4/CHOP Signaling Pathway in Tumor Progression During Endoplasmic Reticulum

Stress. Curr Mol Med 2016, **16**(6): 533–544.

38. Luo J, Xia Y, Luo J, Li J, Zhang C, Zhang H, *et al.* GRP78 inhibition enhances ATF4-induced cell death by the deubiquitination and stabilization of CHOP in human osteosarcoma. Cancer Lett 2017, **410**: 112–123.
39. Yoon MJ, Kang YJ, Lee JA, Kim IY, Kim MA, Lee YS, *et al.* Stronger proteasomal inhibition and higher CHOP induction are responsible for more effective induction of paraptosis by dimethoxycurcumin than curcumin. Cell Death Dis 2014, **5**(3): e1112.
40. Dilshara MG, Neelaka Molagoda IM, Prasad Tharanga Jayasooriya RG, Choi YH, Park C, Kim GY. Indirubin-3'-monoxime induces paraptosis in MDA-MB-231 breast cancer cells by transmitting Ca(2+) from endoplasmic reticulum to mitochondria. Arch Biochem Biophys 2021, **698**: 108723.
41. Chen MS, Wang SF, Hsu CY, Yin PH, Yeh TS, Lee HC, *et al.* CHAC1 degradation of glutathione enhances cystine-starvation-induced necroptosis and ferroptosis in human triple negative breast cancer cells via the GCN2-eIF2α-ATF4 pathway. Oncotarget 2017, **8**(70): 114588–114602.
42. Crawford RR, Prescott ET, Sylvester CF, Higdon AN, Shan J, Kilberg MS, *et al.* Human CHAC1 Protein Degrades Glutathione, and mRNA Induction Is Regulated by the Transcription Factors ATF4 and ATF3 and a Bipartite ATF/CRE Regulatory Element. J Biol Chem 2015, **290**(25): 15878–15891.
43. Chen J, Zaal EA, Berkers CR, Ruijtenbeek R, Garssen J, Redegeld FA. Omega-3 Fatty Acids DHA and EPA Reduce Bortezomib Resistance in Multiple Myeloma Cells by Promoting Glutathione Degradation. Cells 2021, **10**(9).
44. Sung H, Ferlay J, Siegel RL, Laversanne M, Soerjomataram I, Jemal A, *et al.* Global Cancer Statistics 2020: GLOBOCAN Estimates of Incidence and Mortality Worldwide for 36 Cancers in 185 Countries. CA Cancer J Clin 2021, **71**(3): 209–249.
45. Peto R, Davies C, Godwin J, Gray R, Pan HC, Clarke M, *et al.* Comparisons between different polychemotherapy regimens for early breast cancer: meta-analyses of long-term outcome among 100,000 women in 123 randomised trials. Lancet 2012, **379**(9814): 432–444.
46. Bukowski K, Kciuk M, Kontek R. Mechanisms of Multidrug Resistance in Cancer Chemotherapy. Int J Mol Sci 2020, **21**(9).
47. Odaimi M, Ajani J. High-dose chemotherapy. Concepts and strategies. Am J Clin Oncol 1987, **10**(2): 123–132.
48. Prieto-Callejero B, Rivera F, Fagundo-Rivera J, Romero A, Romero-Martín M, Gómez-Salgado J, *et al.* Relationship between chemotherapy-induced adverse reactions and health-related quality of life in patients with breast cancer. Medicine (Baltimore) 2020, **99**(33): e21695.
49. Dinić J, Efferth T, García-Sosa AT, Grahovac J, Padrón JM, Pajeva I, *et al.* Repurposing old drugs to fight multidrug resistant cancers. Drug Resist Updat 2020, **52**: 100713.
50. Sleire L, Førde HE, Netland IA, Leiss L, Skeie BS, Enger P. Drug repurposing in cancer. Pharmacol Res 2017, **124**: 74–91.
51. Jeon KI, Byun MS, Jue DM. Gold compound auranofin inhibits IkappaB kinase (IKK) by modifying Cys-179 of IKKbeta subunit. Exp Mol Med 2003, **35**(2): 61–66.

52. Tanaka M, Fuentes ME, Yamaguchi K, Durnin MH, Dalrymple SA, Hardy KL, *et al.* Embryonic lethality, liver degeneration, and impaired NF-kappa B activation in IKK-beta-deficient mice. Immunity 1999, **10**(4): 421–429.
53. Kim NH, Park HJ, Oh MK, Kim IS. Antiproliferative effect of gold(I) compound auranofin through inhibition of STAT3 and telomerase activity in MDA-MB 231 human breast cancer cells. BMB Rep 2013, **46**(1): 59–64.
54. Takeda K, Noguchi K, Shi W, Tanaka T, Matsumoto M, Yoshida N, *et al.* Targeted disruption of the mouse Stat3 gene leads to early embryonic lethality. Proc Natl Acad Sci U S A 1997, **94**(8): 3801–3804.
55. Wang Y, Hill KS, Fields AP. PKCι maintains a tumor-initiating cell phenotype that is required for ovarian tumorigenesis. Mol Cancer Res 2013, **11**(12): 1624–1635.
56. Seidl S, Braun U, Roos N, Li S, Lüdtke TH, Kispert A, *et al.* Phenotypical analysis of atypical PKCs in vivo function display a compensatory system at mouse embryonic day 7.5. PLoS One 2013, **8**(5): e62756.
57. Panieri E, Santoro MM. ROS homeostasis and metabolism: a dangerous liason in cancer cells. Cell Death Dis 2016, **7**(6): e2253.
58. De Benedetti A, Harris AL. eIF4E expression in tumors: its possible role in progression of malignancies. Int J Biochem Cell Biol 1999, **31**(1): 59–72.
59. Dong C, Zhang L, Sun R, Liu J, Yin H, Li X, *et al.* Role of thioredoxin reductase 1 in dysplastic transformation of human breast epithelial cells triggered by chronic oxidative stress. Sci Rep 2016, **6**: 36860.
60. Hideshima T, Richardson P, Chauhan D, Palombella VJ, Elliott PJ, Adams J, *et al.* The proteasome inhibitor PS-341 inhibits growth, induces apoptosis, and overcomes drug resistance in human multiple myeloma cells. Cancer Res 2001, **61**(7): 3071–3076.
61. Landis-Piwowar KR, Milacic V, Chen D, Yang H, Zhao Y, Chan TH, *et al.* The proteasome as a potential target for novel anticancer drugs and chemosensitizers. Drug Resist Updat 2006, **9**(6): 263–273.
62. Du Y, Zhang H, Lu J, Holmgren A. Glutathione and glutaredoxin act as a backup of human thioredoxin reductase 1 to reduce thioredoxin 1 preventing cell death by aurothioglucose. J Biol Chem 2012, **287**(45): 38210–38219.
63. Mandal PK, Schneider M, Kölle P, Kuhlencordt P, Förster H, Beck H, *et al.* Loss of thioredoxin reductase 1 renders tumors highly susceptible to pharmacologic glutathione deprivation. Cancer Res 2010, **70**(22): 9505–9514.
64. Huang Z, Wu Y, Zhou X, Xu J, Zhu W, Shu Y, *et al.* Efficacy of therapy with bortezomib in solid tumors: a review based on 32 clinical trials. Future Oncol 2014, **10**(10): 1795–1807.
65. Raninga PV, Di Trapani G, Vuckovic S, Tonissen KF. TrxR1 inhibition overcomes both hypoxia-induced and acquired bortezomib resistance in multiple myeloma through NF-κβ inhibition. Cell Cycle 2016, **15**(4): 559–572.

66. Starheim KK, Holien T, Misund K, Johansson I, Baranowska KA, Sponaas AM, *et al.* Intracellular glutathione determines bortezomib cytotoxicity in multiple myeloma cells. Blood Cancer J 2016, **6**(7): e446.
67. Poet GJ, Oka OB, van Lith M, Cao Z, Robinson PJ, Pringle MA, *et al.* Cytosolic thioredoxin reductase 1 is required for correct disulfide formation in the ER. Embo j 2017, **36**(5): 693–702.
68. Chakravarthi S, Bulleid NJ. Glutathione is required to regulate the formation of native disulfide bonds within proteins entering the secretory pathway. J Biol Chem 2004, **279**(38): 39872–39879.
69. Bien M, Longen S, Wagener N, Chwalla I, Herrmann JM, Riemer J. Mitochondrial disulfide bond formation is driven by intersubunit electron transfer in Erv1 and proofread by glutathione. Mol Cell 2010, **37**(4): 516–528.
70. Livak KJ, Schmittgen TD. Analysis of relative gene expression data using real-time quantitative PCR and the 2(-Delta Delta C(T)) Method. *Methods* 2001, **25**(4): 402–408.

Figures

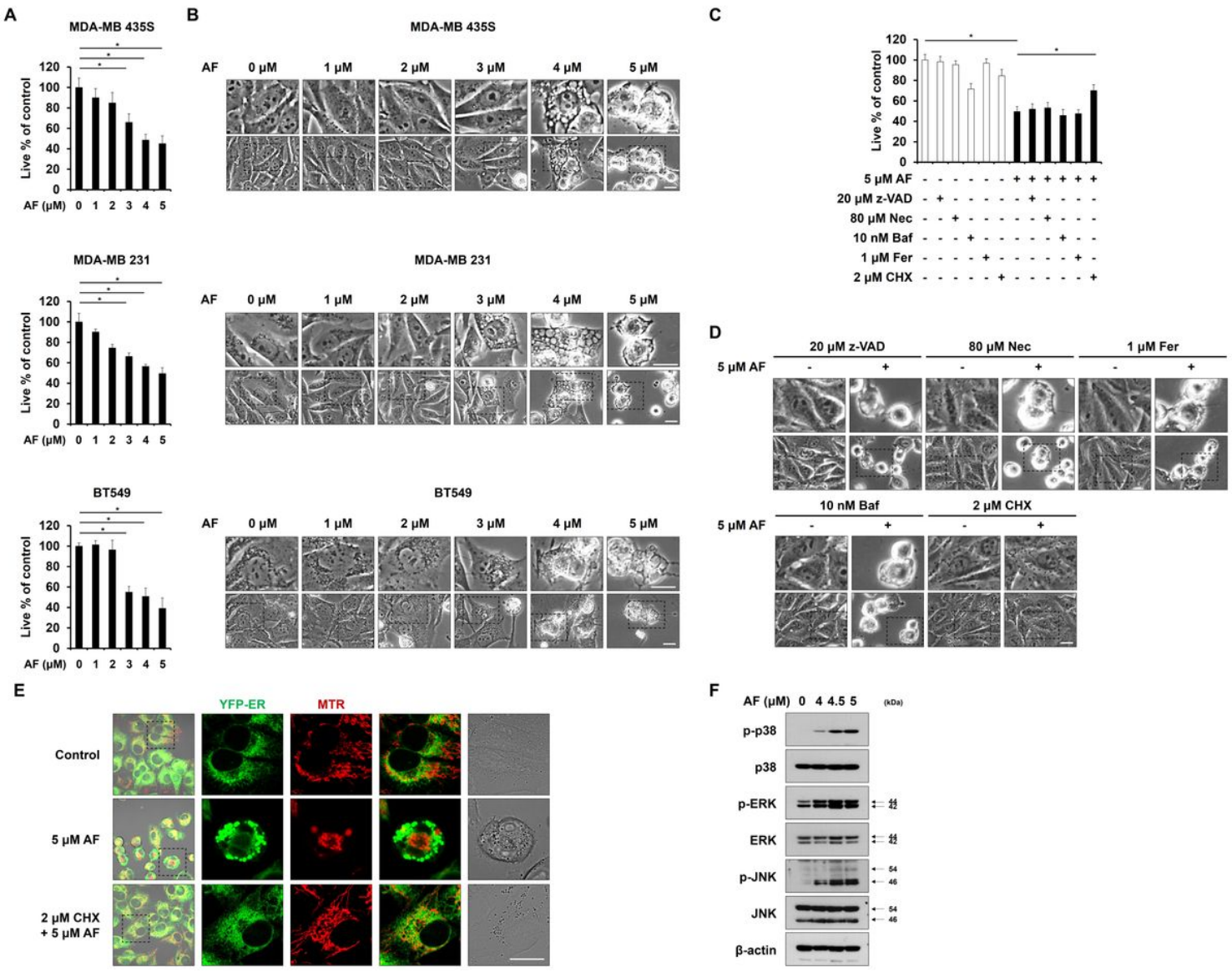

Figure 1

Auranofin induces paraptosis in several breast cancer cell lines.

A, B Cells were treated with the indicated concentrations of AF for 24 h. **C, D** MDA-MB 435S cells pretreated with the indicated doses of z-VAD-fmk (z-VAD), necrostatin-1 (Nec), ferrostatin-1 (Fer), 3-methyladenine (3-MA), bafilomycin A1 (Baf), or cycloheximide (CHX) were further treated with 5 μM AF for 24 h. **A, C** Cellular viability was assessed using IncuCyte, as described in the Materials and Methods. The percentage of live cells was normalized to that of untreated cells (100%). Data represent the means ± SD. (n = 9). One way-ANOVA and Bonferroni's post hoc test. * $p < 0.01$. **B, D** Cellular morphologies were observed by phase-contrast microscopy. Bars, 20 μm. **E** YFP-ER cells treated with 5 μM AF and/or 2 μM CHX for 24 h were stained with MitoTracker-Red (MTR). Cells were observed by confocal microscopy. Bars, 20 μm. **F** MDA-MB 435S cells were treated with the indicated concentrations of AF for 12 h, and Western blotting of the indicated proteins was performed using β-actin as a loading control.

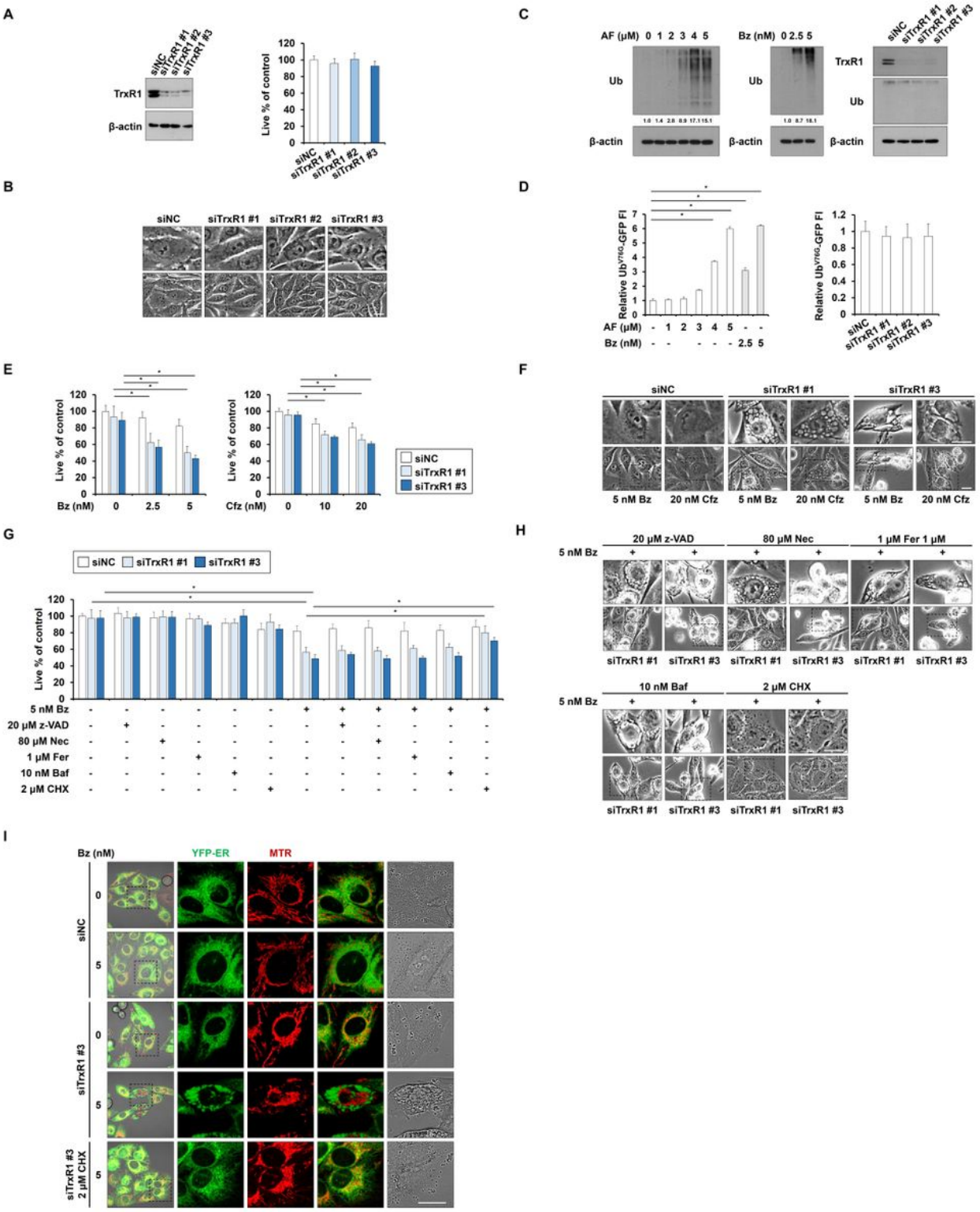

Figure 2

TrxR1/proteasome inhibition is required for AF-induced paraptosis.

A-C MDA-MB 435S cells were transfected with negative control siRNA (siNC) or three different siRNAs against TrxR1 (siTrxR1) for 24 h. **A** Knockdown of TrxR1 was confirmed by Western blotting with β-actin used as a loading control (*left*). Cellular viability in transfected cells was assessed using IncuCyte, as

described in the Materials and Methods. The percentage of live cells was normalized to that of untreated cells (100%). Data represent the means ± SD. (*n* = 9). One way-ANOVA and Bonferroni's post hoc test (*right*). **B** Morphologies of the transfected cells were observed by phase-contrast microscopy. Bars, 20 μm. **C** MDA-MB 435S cells were treated with the indicated concentrations of AF (*left*) or Bz (*middle*) for 12 h. Cells were transfected with siNC or siTrxR1 for 24 h (*right*). Western blotting of the ubiquitinated proteins was performed using β-actin as a loading control. **D** MDA-MB 435S cells transfected with Ub^{G76V}-GFP were treated with the indicated concentrations of AF or Bz for 12 h (*left*). MDA-MB 435S cells were co-transfected with Ub^{G76V}-GFP and siTrxR1 for 24 h (*right*). The fluorescence intensity was assessed, as described in the Materials and Methods. **E, F** MDA-MB 435S cells were transfected with siNC or siTrxR1 for 24 h and further treated with the indicated doses of Bz or Cfz. **G, H** MDA-MB 435S cells were transfected with siNC or siTrxR1 for 24 h, pretreated with the indicated doses of z-VAD, Nec, Fer, 3-MA, Baf, or CHX, and further treated with 5 nM Bz for 24 h. **E, G** Cellular viability was assessed using IncuCyte, as described in the Materials and Methods. The percentage of live cells was normalized to that of untreated cells (100%). Data represent the means ± SD. (*n* = 9). One way-ANOVA and Bonferroni's post hoc test. * $p < 0.001$ (**E**). * $p < 0.05$ (**G**). **F, H** Cellular morphologies were observed by phase-contrast microscopy. Bars, 20 μm. **I** YFP-ER cells transfected with siNC or siTrxR1 were further treated with 5 nM Bz and/or 2 μM CHX for 24 h and then stained with MTR. Cells were observed by confocal microscopy. Bars, 20 μm.

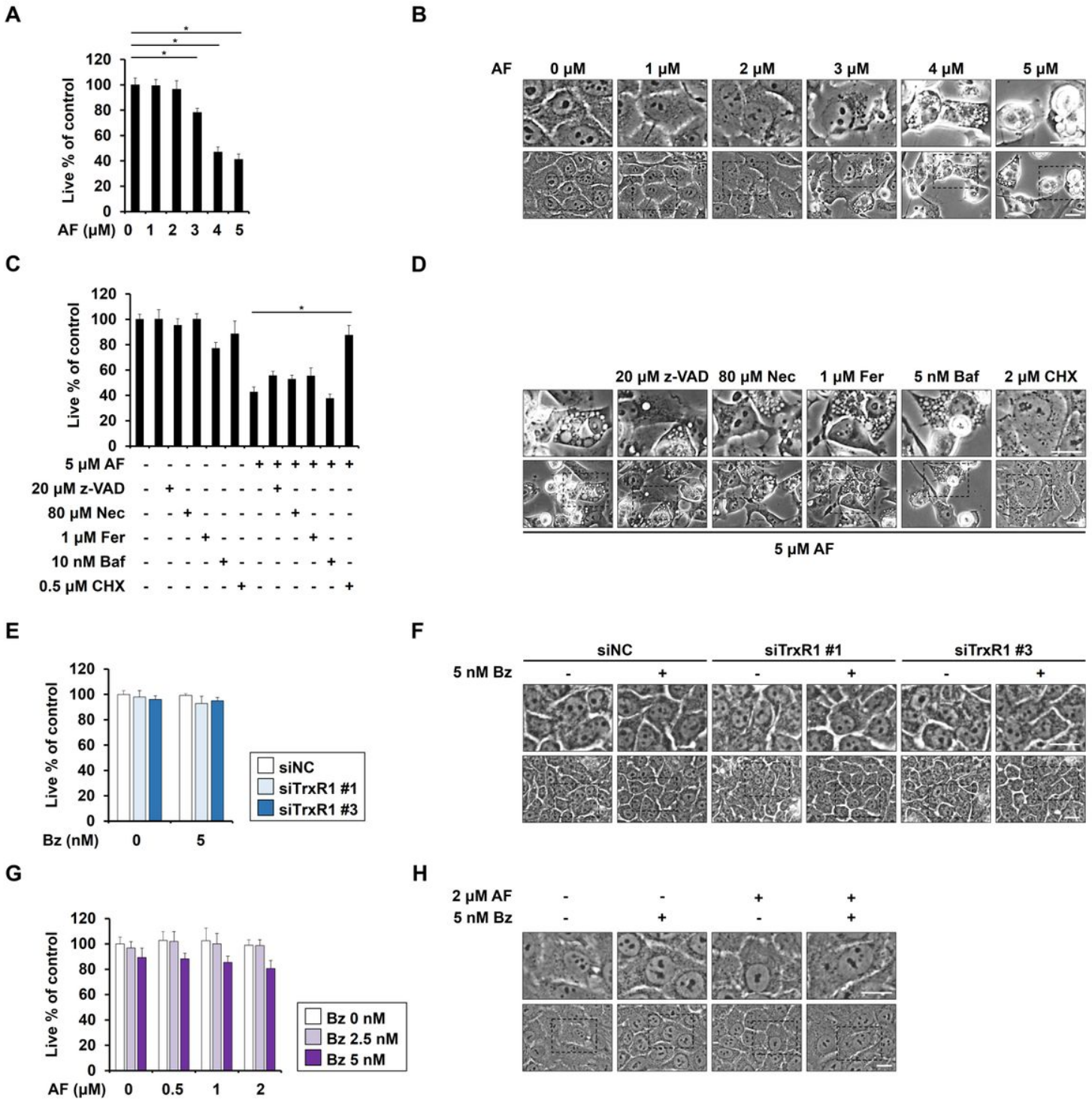

Figure 3

Non-transformed cells are killed by high-dose AF, but spared by TrxR1 knockdown plus Bz or low-dose AF plus Bz.

A, B MCF10A cells were treated with the indicated concentrations of AF for 24 h. **C, D** MCF10A cells pretreated with the indicated doses of z-VAD, Nec, Fer, 3-MA, Baf, or CHX were further treated with AF for 24 h. **E, F** MCF10A cells transfected with siNC or siTrxR1 for 24 h were further treated with the indicated

doses of Bz for 24 h. **G, H** MCF10A cells were treated with the indicated concentrations of AF and/or Bz for 24 h. **A, C, E, G** Cellular viability was assessed using IncuCyte, as described in the Materials and Methods. The percentage of live cells was normalized to that of untreated cells (100%). Data represent the means ± SD. (n = 9). One way-ANOVA and Bonferroni's post hoc test. * $p < 0.001$. **B, D, F, H** Cellular morphologies were observed by phase-contrast microscopy. Bars, 20 μm.

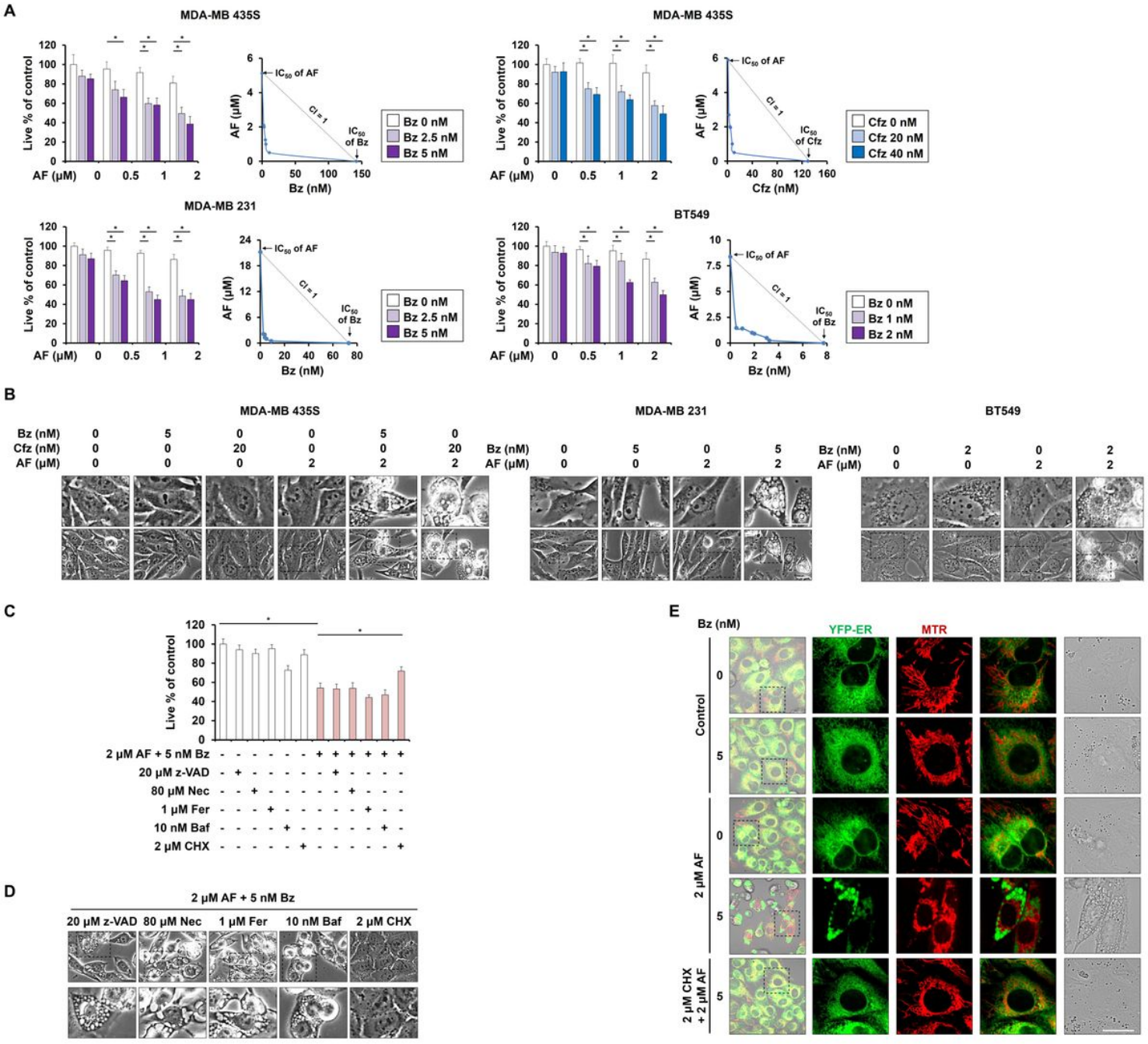

Figure 4

Combining low doses of AF and PI induces paraptosis in breast cancer cells.

A, B Cells were treated with the indicated concentrations of AF and/or PIs for 24 h. **C, D** MDA-MB 435S cells pretreated with the indicated dose of z-VAD, Nec, Fer, 3-MA, Baf, or CHX were further treated with 2

μM AF plus 5 nM Bz for 24 h. **A, C** Cellular viability was assessed using IncuCyte, as described in the Materials and Methods. The percentage of live cells was normalized to that of untreated cells (100%). Data represent the means ± SD. (n = 9). One way-ANOVA and Bonferroni's post hoc test. * $p < 0.05$. **B, D** Cellular morphologies were observed by phase-contrast microscopy. Bars, 20 μm. **E** YFP-ER cells treated with 2 μM AF plus 5 nM Bz and/or 2 μM CHX for 24 h were stained with MTR. Cells were observed by confocal microscopy. Bars, 20 μm.

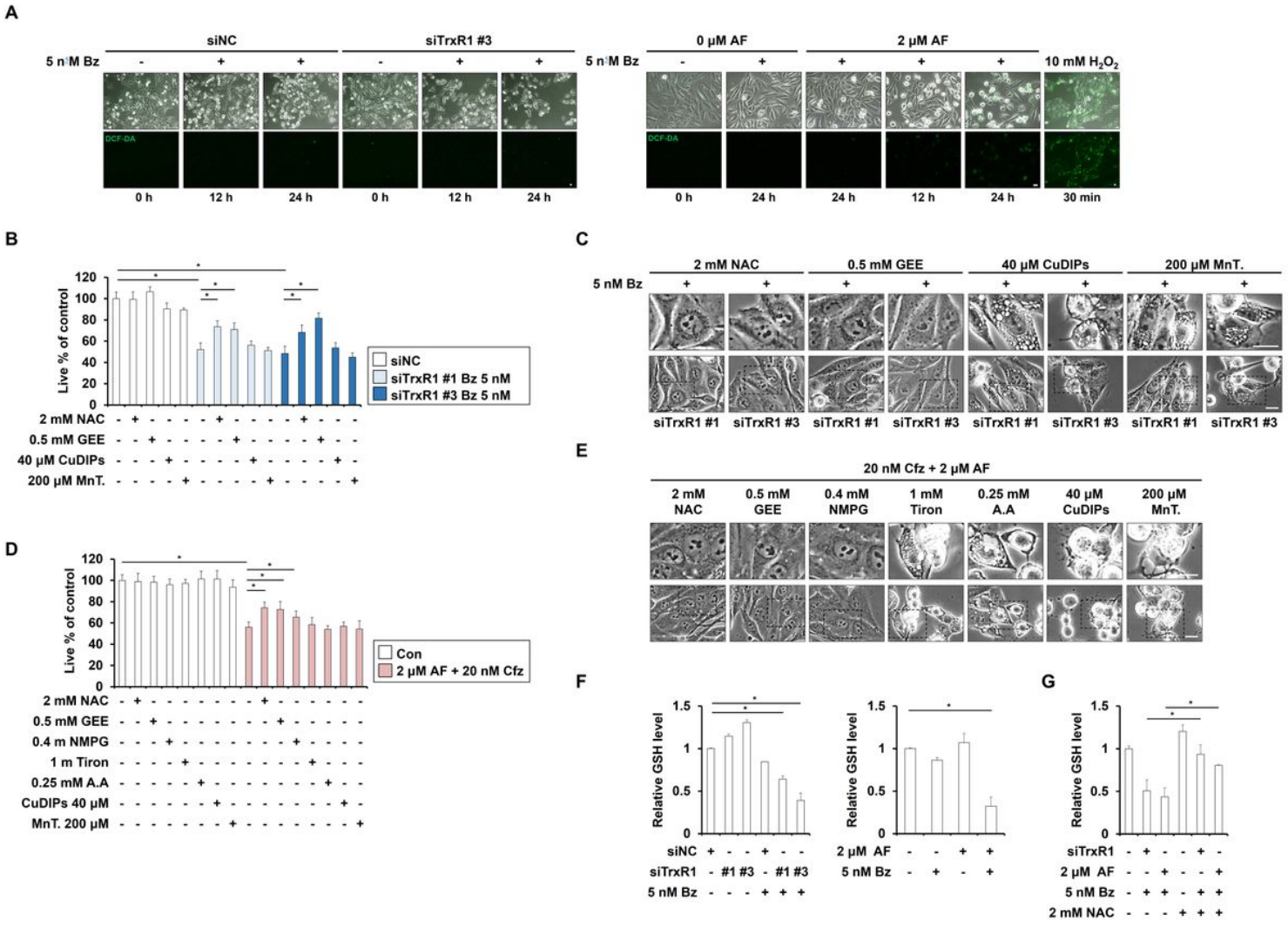

Figure 5

Disruption of thiol homeostasis rather than ROS generation is critical for the paraptosis induced by inhibition of TrxR1 and proteasome.

A MDA-MB 435S cells were transfected with siNC or siTrxR1 and further treated with 5 nM Bz for the indicated duration, or treated with the indicated concentrations of Bz and/or AF or H_2O_2 for the indicated duration. Treated cells were incubated with CM-H_2DCF-DA (DCF-DA) and subjected to fluorescence microscopy. Bars, 20 μm. **B, C** MDA-MB 435S cells transfected with siNC or siTrxR1 were treated with the indicated doses of N-acetylcysteine (NAC), glutathione reduced ethyl ester (GEE), Cu(II)(3,5-

diisopropylsalicylate)2 (CuDIPs), or manganese (III) tetrakis (4-benzoic acid) porphyrin chloride (MnTBAP; MnT) and further treated with 5 nM Bz for 24 h. **D, E** MDA-MB 435S cells were pretreated with the indicated doses of NAC, GEE, N-(2-mercapto-propionyl)-glycine (NMPG), tiron, ascorbic acid (AA), CuDIPs, or MnT and further treated with 20 nM Cfz plus 2 μM AF for 24 h. **B, D** Cellular viability was assessed using IncuCyte, as described in the Materials and Methods. The percentage of live cells was normalized to that of untreated cells (100%). Data represent the means ± SD. (*n* = 9). One way-ANOVA and Bonferroni's post hoc test. * $p < 0.05$. **C, E** Cellular morphologies were observed by phase-contrast microscopy. Bars, 20 μm. **F** MDA-MB 435S cells transfected with siNC or siTrxR1 were further treated with 5 nM Bz for 12 h (*left*) or treated with 5 nM Bz plus 2 μM AF for 12 h (*right*). **G** MDA-MB 435S cells transfected with siNC or siTrxR1 were treated with 2 mM NAC and/or 5 nM Bz for 12 h, or treated with 2 mM NAC and/or AF plus Bz at the indicated concentrations for 12 h. **F, G** GSH levels were assessed, as described in the Materials and Methods.

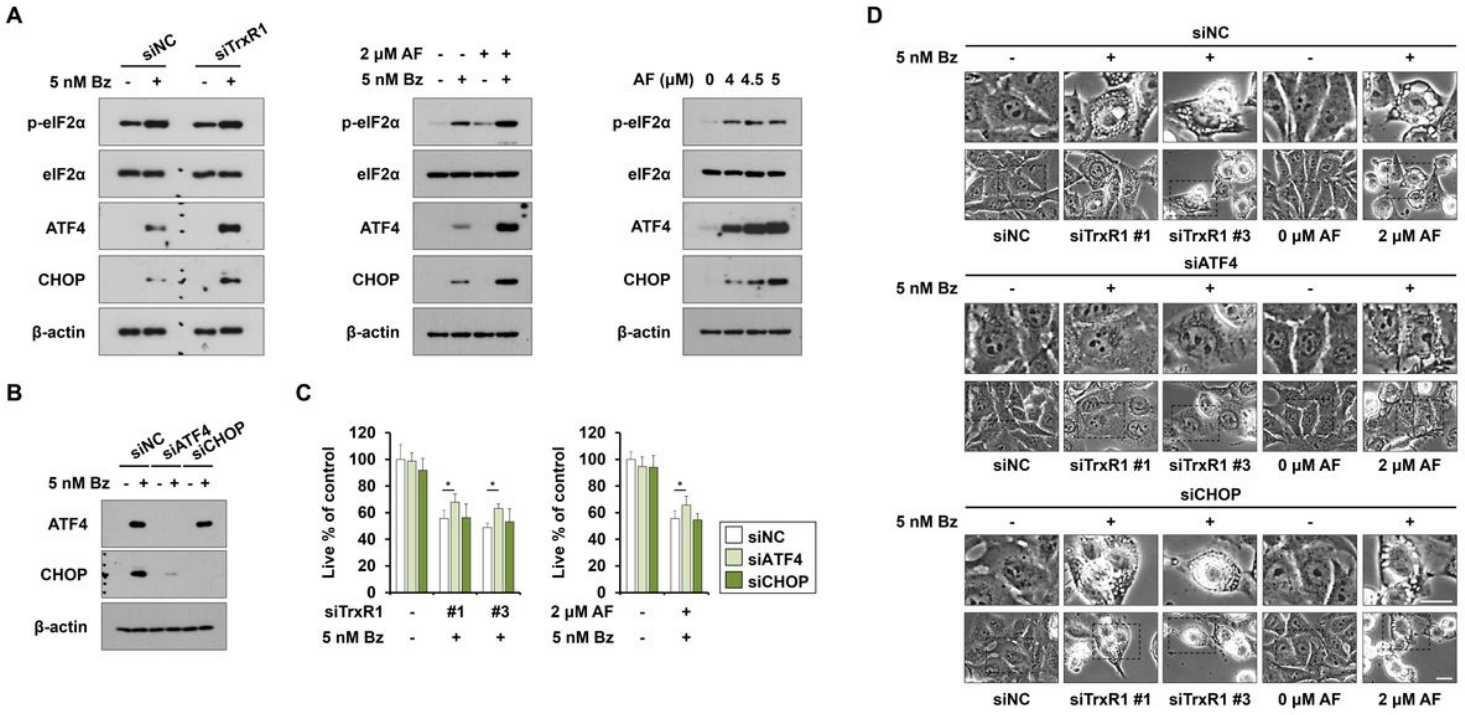

Figure 6

AF-mediated TrxR1 inhibition enhances Bz-induced ER stress, and ATF4 plays a critical role in the paraptosis induced by TrxR1/proteasome inhibition.

A MDA-MB 435S cells transfected with siNC or siTrxR1 were treated with 5 nM Bz for 12 h, or with the indicated concentrations of Bz and/or AF for 12 h. **B-D** MDA-MB 435S cells transfected with siNC, ATF4-targeting siRNA (siATF4), or CHOP-targeting siRNA (siCHOP) were transfected with TrxR1 and further treated with 5 nM Bz for 24 h, or treated with the indicated concentrations of Bz and/or AF for 24 h. **A, B** Western blotting of the indicated proteins was performed using β-actin as a loading control. **C** Cellular viability was assessed using IncuCyte, as described in the Materials and Methods. The percentage of live

cells was normalized to that of untreated cells (100%). Data represent the means ± SD. (n = 9). One way-ANOVA and Bonferroni's post hoc test. * $p < 0.05$. **D** Cellular morphologies were observed by phase-contrast microscopy. Bars, 20 μm.

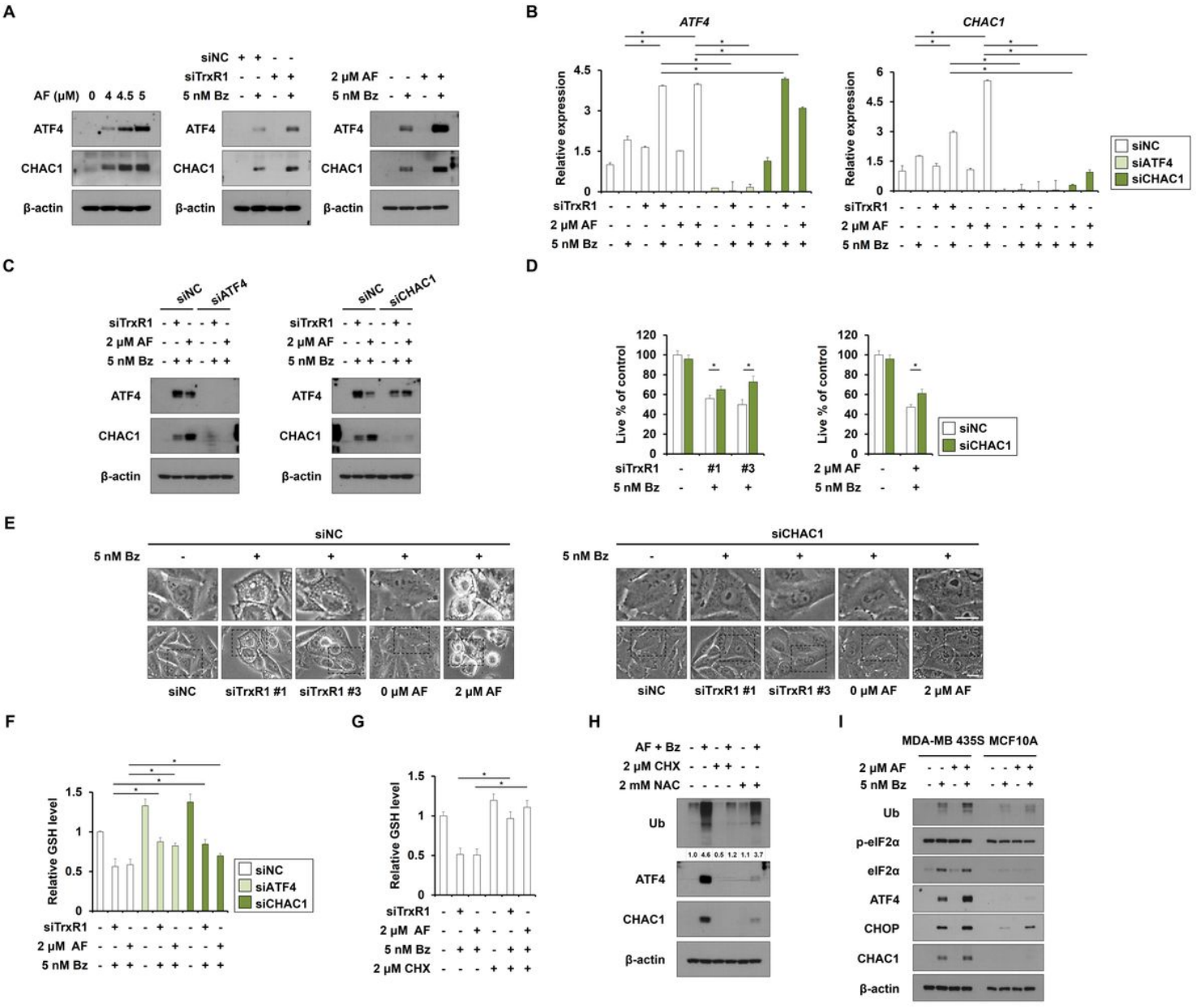

Figure 7

ATF4/CHAC1 critically contributes to the paraptosis induced by TrxR1/proteasome inhibition by degrading GSH

A MDA-MB 435S cells were treated with the indicated concentrations of AF alone (*left*) or Bz and/or AF (*right*) for 12 h. MDA-MB 435S cells transfected with siNC or siTrxR1 were treated with 5 nM Bz for 12 h (*middle*). **B-F** MDA-MB 435S cells transfected with siNC, siATF4, or CHAC1-targeting siRNA (siCHAC1) were cotransfected with TrxR1 and further treated with 5 nM Bz for 24 h, or treated with the indicated concentrations of Bz and/or AF for 24 h. **G, H** MDA-MB 435S cells pretreated with 2 μM CHX or 2 mM

NAC were treated with 2 μM AF plus 5 nM Bz for 12 h. **I** Cells were treated with 5 nM Bz and/or 2 μM AF for 12 h. **A, C, H, I** Western blotting of the indicated proteins was performed using β-actin as a loading control. **B** The mRNA levels of ATF4 or CHAC1 were assessed by qRT-PCR. **D** Cellular viability was assessed using IncuCyte, as described in the Materials and Methods. The percentage of live cells was normalized to that of untreated cells (100%). Data represent the means ± SD. (*n = 9*). One way-ANOVA and Bonferroni's post hoc test. * $p < 0.05$. **E** Cellular morphologies were observed by phase-contrast microscopy. Bars, 20 μm. **F, G** GSH levels were assessed, as described in Materials and Methods.

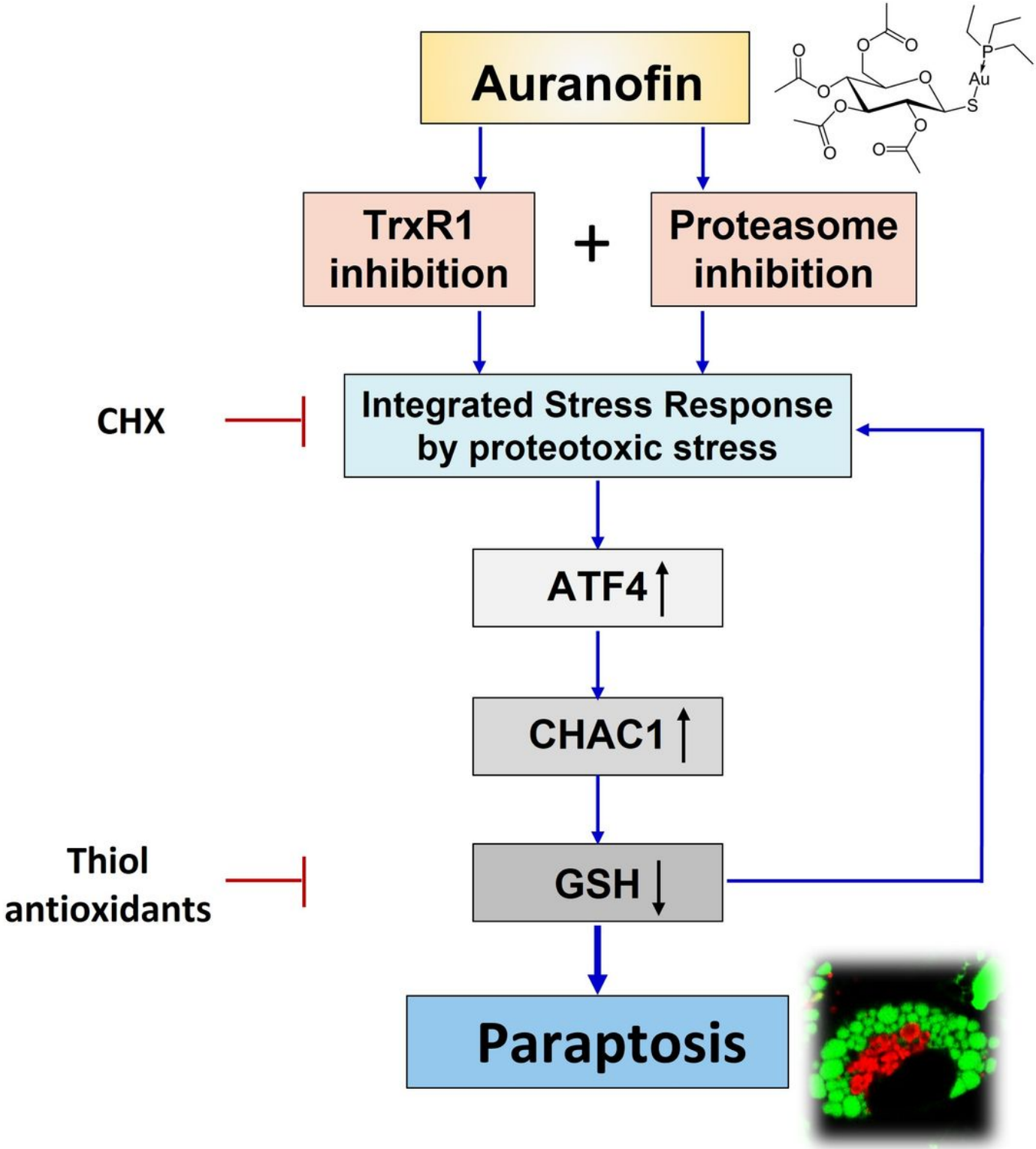

Figure 8

Hypothetical model for the mechanism underlying the paraptosis induced by high-dose auranofin or simultaneous inhibition of TrxR1 and proteasome.

For the induction of auranofin-induced paraptosis, both TrxR1 inhibition and proteasome inhibition are required. Simultaneous TrxR1/proteasome inhibition triggers the ISR due to proteotoxic stress. In this process, GSH degradation, which is mediated by the ATF4/CHAC1 axis, critically contributes to inducing paraptosis by aggravating proteotoxic stress.

Supplementary Files

This is a list of supplementary files associated with this preprint. Click to download.

- SupplementaryInformation.docx
- Supplementarytable1.docx